

Multi-Degree-of-Freedom Precision Position Sensing and Motion Control Using Two-Axis Hall-Effect Sensors

Yusuke Kawato

Won-jong Kim¹

Mem. ASME

e-mail: wjkim@tamu.edu

Department of Mechanical Engineering,
Texas A&M University,
College Station, TX 77843-3123

This paper presents a novel precision position-sensing methodology using two-axis Hall-effect sensors, where the absolute multi-degree-of-freedom (DOF) positioning of a device above any magnet matrix is possible. Magnet matrices have a periodic magnetic field about each of its orthogonal axes, which can be modeled using Fourier series. This position-sensing methodology was implemented on a Halbach-magnet-matrix-based magnetic-levitation (maglev) stage. It enables unrestricted translational and rotational ranges in planar motions with a potential 6-DOF motion-measuring capability. A Gaussian least-squares differential-correction (GLSDC) algorithm was developed and implemented to estimate the maglev stage's position and orientation in three planar DOFs from raw Hall-effect-sensor measurements. Experimental results show its position resolution of better than 10 μm in translation and 100 μrad in rotation. The maximum rotational range achieved so far is 16 deg, a factor of 100 improvement of a typical laser interferometers' rotational range of a few milliradians. Classical lead-lag compensators were designed and implemented on a digital signal processor (DSP) to close the control loop at a sampling frequency of 800 Hz for the three planar DOFs using the GLSDC outputs. Calibration was performed by comparing the Hall-effect sensors' outputs against the laser-interferometer readings, which improved the positioning accuracy by correcting the GLSDC error. The experimental results exhibit better than a micrometer repeatability. This multi-DOF sensing mechanism is an excellent cost-effective solution to planar micro-positioning applications with unrestricted three-axis travel ranges. [DOI: 10.1115/1.2363201]

Keywords: Hall-effect sensor, precision positioning, precision motion control, multi-dimensional positioner, Gaussian least squares differential correction

1 Introduction

To precisely position wafer steppers, surface motors, magnetic suspension stages, or long-range scanning stages, conventional methods use mainly laser interferometers supplemented with optical sensors or capacitance gauges [1–6]. They have high resolution and low positioning noise, allowing sub-nanometer position measurement. However, they have downsides in cost, fine-finish requirement, limitation in travel range, and relative sensing [7].

¹Corresponding author.

Contributed by the Dynamic Systems, Measurement, and Control Division of ASME for publication in the JOURNAL OF DYNAMIC SYSTEMS, MEASUREMENT, AND CONTROL. Manuscript received May 11, 2005; final manuscript received March 6, 2006. Assoc. Editor: Santosh Devasia.

Components of the laser interferometry, such as mirrors, laser heads, and laser interferometers, and electronics add up to be very expensive. They also need a flat reference surface, where the laser beam reflects to the laser receiver to acquire the position data. The mirrors may become very long and bulky to achieve long travel range, which makes the levitated moving part, namely, the platen, heavy and consequently affecting its performance and design. Since the laser beam reflected off the mirror must go into the laser receiver, even small rotations on the order of a few milliradians can make the laser beam stray off the receiver. Then, the moving platen may go unstable due to the loss of feedback signals. This becomes more problematic when applying large (greater than a few millimeters) step inputs because this can generate abrupt reactive jerk on the platen, forcing the platen to rotate enough to cause instability. Moreover, the laser interferometers can only give relative position information by counting fringe patterns without being able to tell the absolute position.

Whereas photolithography requires nanometer-precision positioning with only a few-milliradian rotational range, microassembly without requiring nanometer resolution may benefit from larger angular motion capabilities that cannot be met with conventional laser interferometers. Further, micro-assembly processes require absolute micrometer precision positioning, for it must follow the identical trajectory in the absolute reference frame. Unlike the precision positioning stages presented in [3–5], the maglev stage used in this research [2] has potential large angular motion capabilities in the XY plane. However, its performance could not have been demonstrated previously due to the above-mentioned limitations of the laser interferometers.

Considering the capabilities of our maglev device and the need for a device with unrestricted translational and rotational range, we sought for a novel sensing method with sufficient position resolution, while allowing large rotation and absolute position measurement. We focused on the periodicity of the magnetic field generated by the magnet matrix, which can be measured by magnetic-field sensors such as Hall-effect sensors.

By deriving an algorithm to estimate the position and orientation of the platen by measuring the magnetic flux density, we could control the platen. Hall-effect sensors are used in various applications, for they are contactless, small in size, reliable, low-cost, linear, and not sensitive to harsh and polluted environmental conditions. However, they are limited in accuracy due to offset, noise, temperature, and aging effects [8]. These downsides can be overcome by calibration and implementation of appropriate filters. Hall-effect sensors have been utilized in various measurement techniques, such as current sensing [9], sensing the movement of ferrous metal targets, and measuring position of rotating machinery [10]. Previous work showed their capability in sensing rotations of less than one degree [11].

In this paper, we develop a novel precision sensing methodology for multi-DOF positioning with two-axis Hall-effect sensors. The primary purpose of this research is to develop a sensing mechanism that can provide position feedback when the laser interferometer system fails, which could happen easily due to large rotational and translational motion or obstacles in the laser path. Implementing this absolute sensing mechanism is sufficient for micrometer-order precision positioning. At the same time it will increase the rotational travel range of the platen and have unrestricted translational motion range, which are key requirements for repetitive motion in micro-assembly.

This approach has many attractive features including (1) very small ($5.0 \times 6.0 \times 1.6$ mm) sensors for unrestricted planar (X , Y , and θ_z) motion detection, (2) no costly laser-interferometer setup required (each two-axis Hall-effect sensor is \$10), (3) relatively simple electronic circuits with no demanding design constraints, and (4) sub-100-microradian rotational resolution with micrometer-order translational resolution.

This paper is organized as follows. First, the magnetic characteristics of the concentrated-field Halbach magnet matrix [1,12]

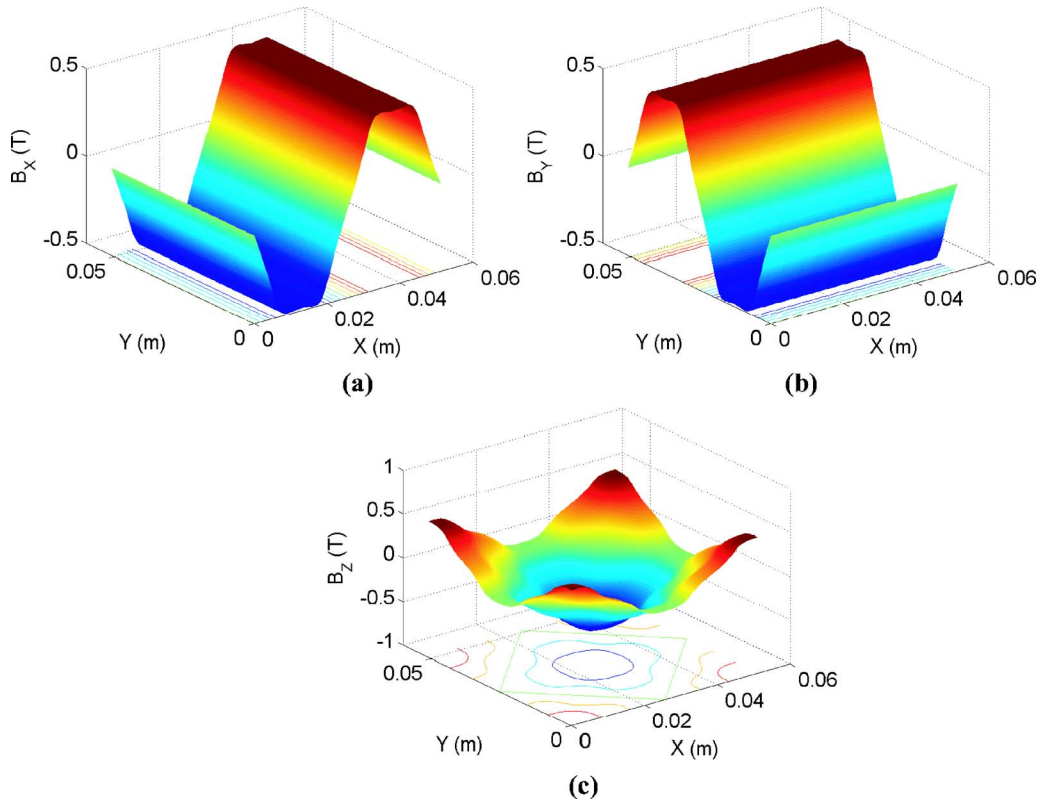


Fig. 1 Analytical results of the magnetic flux density generated by the Halbach magnet matrix at an air gap of $Z_0=3$ mm. (a) B_x , (b) B_y , and (c) B_z .

are provided in Sec. 2. In Sec. 3, the sensing mechanism and the position-estimation methodology are described. Three sets of two-axis Hall-effect sensors are used for 3 DOF positioning in a plane. Section 4 describes the GLSDC-based multi-axis position-sensing algorithm. The electromechanical setup for the test bed is illustrated in Sec. 5. Based on the dynamic model of the maglev stage and its controllers designed in Sec. 6, 2 DOF and 3 DOF positioning experimental results are presented and discussed in Sec. 7.

2 Halbach Magnet Matrix Analysis

To enhance the understanding of our proposed sensing mechanism, we describe in this section the nature of the 3-D magnetic field generated by the Halbach magnet matrix [1,2,12]. This magnet matrix is a superposition of two orthogonal Halbach magnet arrays with orthogonal magnetic fields. Halbach arrays have a stronger fundamental field by a factor of $\sqrt{2}$, which allows a design of a higher power-efficient magnetic device [13]. This concentrated-field magnet matrix consists of two kinds of magnets differing in magnetization. One is a strong magnet with 90 deg magnetization, where we chose NdFeB50 material with remanence of $B_{r, \text{strong}}=1.43$ T. The other magnet used is a weak magnet with magnetization in 45 deg. NdFeB30 material with a remanence of $B_{r, \text{weak}}=1.10$ T was chosen for the weak magnet, which was the weakest NdFeB material on the market at the time of purchase. The pitch (l) of each magnet array is 50.8 mm (2 in.), and the dimension of each magnet and spacer is $12.7 \times 12.7 \times 12.7$ mm ($0.5 \times 0.5 \times 0.5$ in.).

Due to the periodicity of the magnet matrix, the magnetic flux density \mathbf{B} is modeled using Fourier series. From this analysis, we find that for an ideal Halbach magnet matrix, there are nonzero fundamental, fifth, ninth, ... harmonics, and that other harmonics are zero. For the actual case, the fundamental and fifth-order har-

monics have the largest magnitudes, so we chose these two harmonics as the basis functions. The model of the magnetic flux density at (X, Y, Z_0) is in the form,

$$\begin{aligned}
 B_x(X, Y, Z_0) &= \xi_x + \alpha_x \sin(\gamma_1 X) + \beta_x \sin(\gamma_5 X) + \zeta_x \sin(\gamma_1 Y) \\
 &\quad + \delta_x \sin(\gamma_5 Y) \\
 B_y(X, Y, Z_0) &= \xi_y + \alpha_y \sin(\gamma_1 Y) + \beta_y \sin(\gamma_5 Y) + \zeta_y \sin(\gamma_1 X) \\
 &\quad + \delta_y \sin(\gamma_5 X)
 \end{aligned} \tag{1}$$

where $\gamma_1(=2\pi/l)$ and $\gamma_5(=10\pi/l)$ are the fundamental and fifth spatial wave numbers, and ξ , α , β , ζ , and δ are the parameters to be curve fitted for a fixed air gap Z_0 between the stationary magnet matrix and the moving coils on the platen. The coefficients ζ and δ are included to compensate for the sensor misalignment in the Z axis, and ξ is the DC offset. From our analysis, we obtained the total magnetic flux density in the target area for an air gap of 3 mm, shown in Fig. 1. Its X and Y components are identical but the axes are reversed, as shown in Figs. 1(a) and 1(b), respectively. Both the X -magnet array and the Y -magnet array contribute to the Z component of the total magnetic flux density, as shown in Fig. 1(c). B_x and B_y are not perfectly symmetric in reality due to the magnet-matrix fabrication error, so each axis must be curve fitted. Although higher-order harmonics can be included in the model, its contributions were significantly smaller than the modeling error, and hence were neglected. A batch least-squares method was used for the curve fitting, which will be described in Sec. 4.1.

Extending this magnetic-flux-density analysis to 6 DOF position sensing, the curve-fitted coefficients α , β , ζ , and δ of Eq. (1) can be written in the form,

$$\alpha(Z) = \alpha_0 e^{-\gamma_1 Z}$$

$$\begin{aligned}
\beta(Z) &= \beta_0 e^{-\gamma_5 Z} \\
\zeta(Z) &= \zeta_0 e^{-\gamma_4 Z} \\
\delta(Z) &= \delta_0 e^{-\gamma_3 Z}
\end{aligned}
\tag{2}$$

where α_0 , β_0 , ζ_0 , and δ_0 are the coefficients to be curve fitted. They contain the exponential dependence in Z because the magnetic flux density in Eq. (1) satisfies the Laplace equation [1]. In addition to measuring the magnetic flux density in the X and Y axes, it is necessary to measure the magnetic field in the Z axis. For the case of 6 DOF positioning, it is required to scan the “target area” at various air gaps in order to obtain an appropriate curve-fitted model.

3 Two-Axis Hall-Effect Sensing Mechanism

For our experiment, we designated the “target area” of one pitch by one pitch (50.8×50.8 mm) on the Halbach magnet matrix. First, let us consider a case for positioning within one pitch in 1-D. The platen will move along the X axis where there is a periodic magnetic field B_X generated by the magnet matrix, which can be modeled as a periodic sinusoidal function. On the platen are two Hall-effect sensors that detect the magnetic flux density at two distinct points along the X axis. If there are two Hall-effect sensors positioned with some phase difference, it is possible to detect the unique position of the platen within one pitch, as well as the direction of its motion. Further, if the Hall-effect sensors are located

$$\left(\frac{1}{4} + \frac{1}{2}n\right)l, \quad n = 1, 2, 3, \dots
\tag{3}$$

apart, at least one sensor will be located in a more “sensitive” region where the gradient of B_X (or the Hall voltage, because Hall voltage and magnetic flux density have a linear relation) is large with respect to the position. Position sensing is sensitive in the region where this gradient is large because small motion along the axis will result in a large change in the Hall voltages. In our setup, the sensitive region has a gradient of about 50 mV/mm. Having at least one sensor in the sensitive region allows positioning within the target area to be sensitive everywhere over the whole magnet matrix. Next, let us consider positioning in a 2-D XY plane without rotation. If there are orthogonal magnetic fields in a plane and two independent measurements can be taken for each axis, we can position the platen in 2-D.

Further, the fact that B_X and B_Y are orthogonal brings another advantage. The reason for having two sensors per axis is only to detect the unique position, and these are redundant in terms of DOFs. We can effectively use these four sensor outputs to detect the orientation in θ_z as well as by triangularization with the difference in the sensor readings. Theoretically, it is possible to control the three planar DOFs using two sets of two-axis Hall-effect sensors. However, due to the modeling error of the magnetic flux density and various uncertainties in sensor locations and misalignments, it was difficult to stabilize the platen with only two sensors. Hence, we have incorporated three sets of sensors on the maglev positioner, and a corresponding algorithm has been implemented in our 3 DOF sensing scheme. Similar to the 2 DOF positioning case, having redundant sensors will likely improve the positioning accuracy and is easy to implement. In the following sections, this sensing algorithm is explained thoroughly for a case when three sensors (six sensor outputs) are available for 3 DOF positioning.

An important task in this research is to find a way to map the nonlinear relationship between the six Hall-effect sensors’ outputs and the position and orientation of the platen. Candidate methods for this nonlinear mapping include neural networks [14] and the GLSDC [15]. The GLSDC algorithm was implemented due to its more deterministic nature. Advantages of using the GLSDC algorithm include (1) it incorporates a continuous periodic model, and

the output will be continuous even when the platen goes beyond the target area, and (2) the algorithm can easily be extended when more redundant sensor measurements are available, which will improve the position noise and accuracy because the GLSDC algorithm gives the least-squares solution.

The precision-positioning and motion-control methodology proposed herein is applicable for the positioning of a platen atop any magnetic matrices, such as [12,16–19]. Note that the nonlinear relationship is between the magnetic flux density and the sensors’ output signals, and hence this can be applied for other orthogonal magnet matrices where its periodic magnetic fields can be modeled. For example, the magnet matrices presented in [16–19] can be modeled using Fourier series, similar to Eq. (1). Hence this nonlinear mapping using the GLSDC algorithm can be applied for these matrices as well. In this paper, we deal with positioning of a platen of a unified multi-dimensional positioner with a double-axis Halbach magnet matrix [1,2,12].

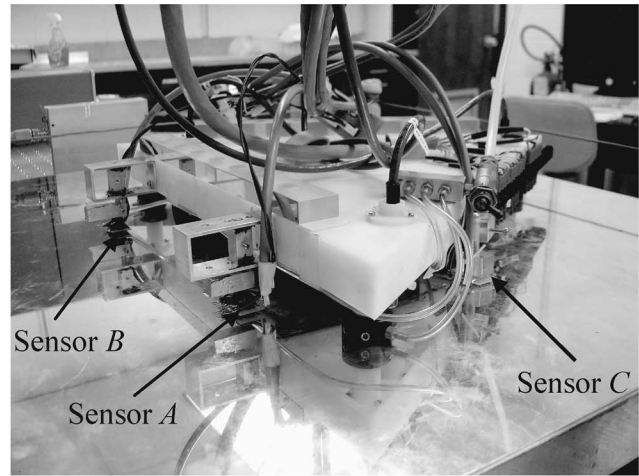
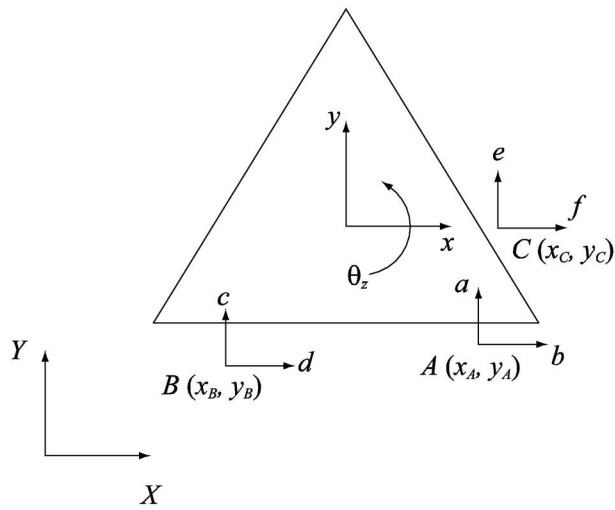
The positioner used in our experiment is capable of positioning in 6 DOFs with 20 nm positioning resolution using laser interferometers for controlling planar DOFs [2]. The platen is currently suspended using three aerostatic bearings and generates force to move in all 6 DOFs using three planar motors attached to the bottom of the platen. Figure 2(a) shows the platen with three sets of two-axis Hall-effect sensors mounted. The sensor fixture was designed such that vertical and rotational adjustments could be made. Below the platen is the Halbach magnet matrix covered with a mirror-finished, 0.8 mm thick aluminum plate. In the following section, the algorithm to determine the platen’s position in three planar DOFs is described.

4 Sensing Algorithm

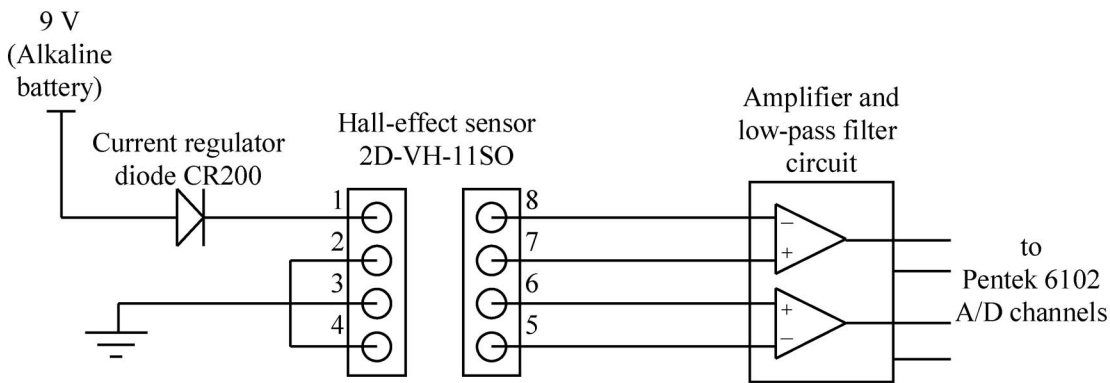
The objective of this section is to show how to resolve the position of the platen from the sensor outputs. Consider a 3 DOF positioning scheme to position the $\{X Y \theta_z\}^T$ axes from the three (A, B, C) two-axis Hall-effect sensors $\{\tilde{a} \tilde{b} \tilde{c} \tilde{d} \tilde{e} \tilde{f}\}^T = \{A_x A_y B_x B_y C_x C_y\}^T$, as shown Fig. 2(a). The tilde ($\tilde{\cdot}$) signifies that they are measured values of the Hall-effect sensors. The GLSDC algorithm is implemented to obtain the position and orientation of the platen in an XY plane at a constant air gap. The GLSDC minimizes the error between the measured output and that from a model, and by doing so estimates the position of the platen. Hence, we must derive an appropriate model of the magnetic flux density for each sensor output first. The model is obtained using the batch least-squares method prior to the experiment, where the raw Hall-effect sensor data are calibrated against the laser interferometers, as explained in the following section.

4.1 Batch Least Squares. Consider the case for the sensor output \tilde{a} as shown in Fig. 3. First, we obtained measurements by scanning the whole “target area,” as shown in Fig. 3(a). To incorporate the Hall-effect sensors’ outputs with respect to the platen’s position, we controlled the platen to follow a zigzag trajectory using the laser interferometers and by doing so measured the magnetic flux density. Using the batch least-squares method, we solved for the curve-fitted model shown in Fig. 3(b). The batch least-squares method solves for the curve-fitting parameters α , β , ζ , δ , and ξ of Eq. (1) for each of the sensor outputs. The values of X and Y are obtained from the laser interferometer readings.

The difference between the measured and modeled values is shown in Fig. 3(c). The maximum variation between the two was less than 200 mV. Possible reasons for this error are (1) fabrication error of the Halbach magnet matrix, (2) error in material properties of the magnets such as the direction of magnetization vector and the remanence of each magnet piece, (3) modeling error of the magnet matrix using the batch least-squares curve-fitting, (4) Hall-effect sensor misalignment with respect to the



(a)



(b)

Fig. 2 Experimental setup with three sets of 2D-VH-11SO 2-axis Hall-effect sensors. The coordinate-axis definition for the experimental setup with the indication of the three two-axis Hall-effect sensors' locations is also given. The actual locations of the three Hall-effect sensors are indicated with arrows. The white triangular Delrin frame is the moving platen. Beneath the mirror-finished aluminum plate is the Halbach magnet matrix. (b) Schematic diagram of the sensing circuit with a 2D-VH-11SO two-axis Hall-effect sensor.

platen's axes in θ_x , θ_y , and θ_z , (5) error in defining the precise location of the sensor (the sensitive volume of the Hall-effect sensor is only $250 \times 250 \times 200 \mu\text{m}$), and (6) interference from external magnetic field and sensor noise. If this modeling error were too large, it might lead the GLSDC to converge to an inaccurate local minimum. To minimize this possibility, precise adjustments in alignment must be made along with a low-noise signal-conditioning circuit for the Hall-effect sensors. This is also why having redundant sensors may be a good idea to improve the position sensing accuracy. Having such a model $\mathbf{f}(\mathbf{x})$ for each sensor output, the mapping between the raw Hall-effect sensor output and the laser interferometers is complete, and we can control the platen with only the Hall-effect sensors. Now we proceed to the GLSDC algorithm.

4.2 Gaussian Least-Squares Differential Correction. The GLSDC solves the nonlinear relation between the position of the platen and the sensors' outputs. A flowchart of the GLSDC algorithm is shown in Fig. 4. At each time step, the measured input signals $\tilde{\mathbf{y}} = \{\tilde{a} \tilde{b} \tilde{c} \tilde{d} \tilde{e} \tilde{f}\}^T$ are obtained, the Jacobian matrix \mathbf{H} is solved, and the GLSDC algorithm is executed to minimize J , the sum square of the residual errors. The Jacobian matrix \mathbf{H} and sum of square of residual errors J are defined as

$$\mathbf{H} = \left. \frac{\partial \mathbf{f}}{\partial \mathbf{x}} \right|_{\mathbf{x}_c} \quad (4)$$

$$J = \Delta \mathbf{y}_c^T \mathbf{W} \Delta \mathbf{y}_c$$

Each iteration, the algorithm calculates the variation $\Delta \mathbf{y}_c$ between the measured sensor output $\tilde{\mathbf{y}}_c$ and the estimated sensor output $\mathbf{f}(\mathbf{x}_c)$. The estimated sensor output is calculated from the estimated location of the platen (\mathbf{x}_c), which is the output of the GLSDC algorithm. The GLSDC algorithm converges correctly when the estimated location of the platen is in the vicinity of the actual position. The sum square of residual errors J checks for the convergence for each iteration. This is a modified GLSDC algorithm of the conventional algorithm presented in [15], where α in Fig. 4 is a scaling factor adjusted to minimize the GLSDC output's oscillation. For our experimental setup, the sensor noise's standard deviation is 1 mV, and selecting $\alpha=0.2$ resulted in the best convergence. The GLSDC algorithm calculates the optimal estimate position recursively. Hence when the controller is activated, if the initial position is far off from the initial estimate position, we empirically know that it takes two to four iterations for both the two- and three-sensor cases.

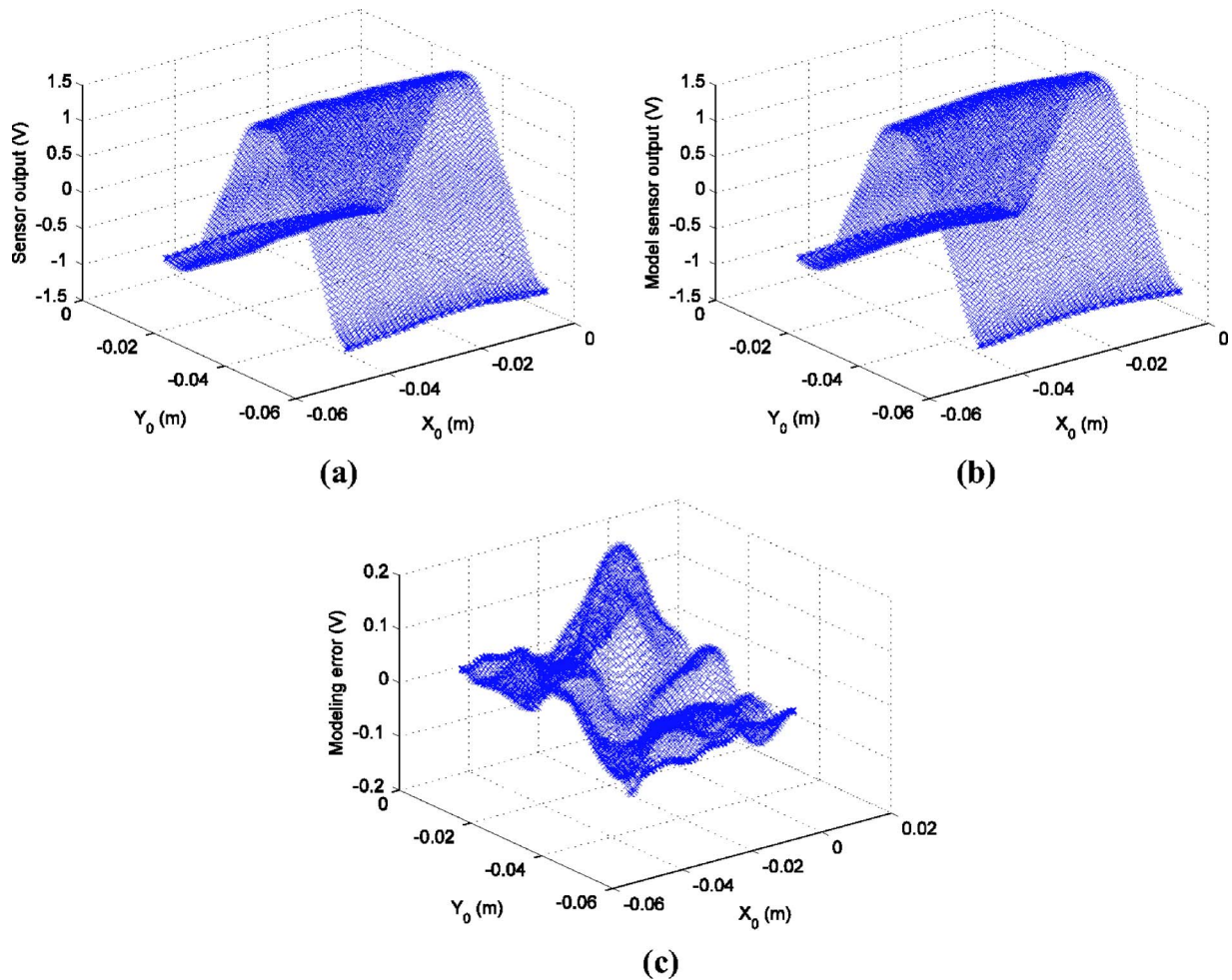


Fig. 3 Batch least-squares results of the magnetic-flux-density measurement. (a) Sensor output \tilde{a} , (b) curve-fitted model for the sensor output \tilde{a} , and (c) modeling error from curve-fitting.

5 Electromechanical Setup

5.1 Mechanical Setup. Photographs of the experimental setup for 3 DOF positioning are shown in Fig. 2(a). The origin of the body-fixed (xyz) coordinate system is attached to the platen's center of mass. The coordinate-axis convention of the Hall-effect-sensor measurements is also shown in the figure. The locations of the three sensors $A(x_A, y_A)$, $B(x_B, y_B)$, and $C(x_C, y_C)$ are known in the body-fixed xyz frame, and a , b , c , d , e , and f are the sensors' outputs. In our current experimental setup, $x_A=89.7$, $y_A=-123.1$, $x_B=-97.1$, $y_B=-136.7$, $x_C=129.8$, and $y_C=11.7$, all in millimeters.

The two-axis Hall-effect sensor used in this research is 2D-VH-1150 manufactured by Sentron AG. It is an eight-pin, surface-mount, small-outline integrated circuit (SOIC). It can measure the magnetic flux density in two orthogonal axes parallel to the chip's surface [8]. Its specifications are given in Table 1. The 2D-VH-1150 requires either a constant current source of 2 mA or a constant voltage source of 5 V. We chose to use a 2 mA current source because it resulted in less sensor noise. Current-regulator diodes CR200 by Vishay Siliconix are used to supply the constant current. The total cost for the sensors, sensor mounts, and sensing and signal-conditioning circuits was less than \$200.

The sensor mounts are fixed to the platen by setscrews and were designed so that minor adjustments could be made to position and align the sensors. The sensors are mounted at three distinct points with respect to the magnetic field's phase of the X and

Y axes to maximize the sensitivity. The surfaces of the Hall-effect sensor chips were positioned close to the surface of the magnet matrix. However, placing them too close would be an additional source of modeling error because unmodeled higher harmonics of the Fourier series would come into play. Thus, the gap between the sensors and the magnet matrix was set to be 2 mm. The sensors' measurement axes were adjusted to align with the platen's body-fixed xyz axes.

5.2 Electronic Setup and Data Acquisition. A schematic diagram of the sensing circuit is shown in Fig. 2(b). The circuit consists of a power supply, a two-axis Hall-effect sensor, a signal amplifier, and a low-pass filter as an antialiasing filter. The outputs of the Hall-effect sensors are amplified by a factor of 21 using operational-amplifier circuits and go through antialiasing filters with a cutoff frequency of 200 Hz. The standard deviation of the sensor output noise after filtering is about 1 mV. There are three sets of this sensing circuit, one for each sensor.

A Pentek 4284 DSP board is used for real-time digital control, and a Pentek 6102 analog-to-digital (A/D) converter board and a Dadel DVME 622 digital-to-analog (D/A) converter board are used for data acquisition and control. In Fig. 2(a), the notations a , b , c , d , e , and f are used for the sensor's outputs after amplification and filtering, which correspond to the labels of the input channels of the Pentek 6102. The GLSDC algorithm is implemented in real-time C codes.

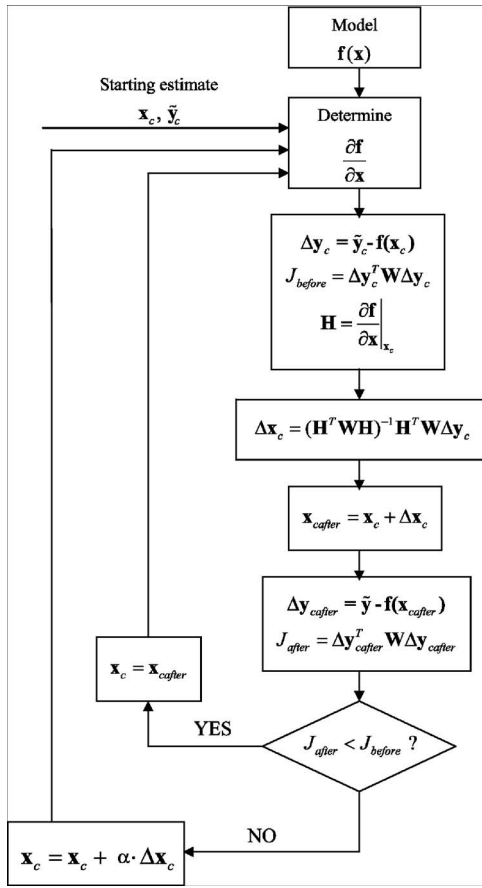


Fig. 4 Flowchart of the modified GLSDC algorithm

6 Dynamic Modeling and Controller Design

A 3-D finite-element (FE) model of the mechanical system was built using SolidWorks. The system parameters such as the platen center of mass, inertia matrix, and natural frequencies were calculated with this FE model. The platen is modeled as a pure mass since there is no mechanical contact, backlash, or hysteresis. The magnetic spring constant and the damping factor are also negligible.

6.1 Plant Transfer Functions. For translational motion, the equation of motion in X is as the following by Newton's second law

$$M \frac{d^2x}{dt^2} = f \quad (5)$$

where M is 6.20 kg. Thus, the open-loop plant transfer function is

$$\frac{X(s)}{F(s)} = \frac{1}{6.20s^2} \quad (6)$$

The open-loop plant transfer function in Y is identical to Eq. (6). Likewise, the open-loop plant transfer function for rotational motion is

$$\frac{\Theta_{zz}(s)}{T(s)} = \frac{1}{I_{zz}s^2} \quad (7)$$

where T refers to the torque about the z axis, and I_{zz} refers to the principal moment of inertia about the z axis calculated as 0.054 kg·m² using SolidWorks.

6.2 Controller Design and Implementation. Three independent lead-lag controllers were designed and implemented for each of the three axes (x , y , and θ_z) to stabilize the planar motion of the maglev system. We used the MATLAB's "sisotool" function to select the control parameters. By using the zeroth-order-hold (ZOH) method with an 800 Hz sampling rate, the following digital lead-lag compensators were designed

$$D_{x,y}(z) = 2.236 \times 10^5 \frac{z^2 - 1.9773z + 0.977428}{z^2 - 1.2423z + 0.2423} \quad (8)$$

$$D_{\theta}(z) = 4.155 \times 10^3 \frac{z^2 - 1.9773z + 0.977428}{z^2 - 1.2423z + 0.2423} \quad (9)$$

Our lead-lag compensators have a significant separation between their lead pole and lead zero, and the phase crossover frequencies are at about 10 Hz for x and y , and 20 Hz for θ_z . Thus the Hall-effect sensors' filter cutoff frequency at 200 Hz was high enough, and their dynamics was neglected.

We implemented these control laws in real-time C on a Pentek 4284 DSP board and developed a user interface on a VME PC (Model 7751 by VMIC) in C++. The whole real-time sensing and control routine is executed every 1.25 ms (i.e., at an 800 Hz sampling frequency).

7 Experimental Results

Experiments were conducted to test the performance of the proposed sensing methodology. First, results for 2 DOF positioning using Hall-effect sensors are presented, where the translational x and y control loops are closed using Hall-effect sensor outputs and the GLSDC algorithm, and the θ_z control loop is closed using the laser interferometers. In the 2 DOF positioning experiments, the GLSDC outputs are compared with the laser interferometer readings to prove the validity of our sensing method. We consider the laser interferometer readings as the "true" values and use it as a comparison to prove our sensing method's accuracy. The laser interferometer setup has a resolution of 0.6 nm. This allowed us to (1) compare the performance between our sensing method and the laser interferometers, (2) calibrate the Hall-effect sensor outputs against the much more accurate laser interferometers, and (3) correct any sensing and GLSDC error by error mapping. Then, for the 3-DOF positioning experiments, laser interferometers are removed and position sensing relies exclusively on the Hall-effect sensors.

7.1 2 DOF Positioning Results. For 2 DOF positioning, two sets of Hall-effect sensors (sensors A and B) were used in the GLSDC algorithm. The platen is controlled in X and Y using solely the estimated position data from the Hall-effect sensors, and meanwhile the position data from the laser interferometers were recorded. The purpose of this experiment is to evaluate the positioning accuracy of our sensing method by comparing with that of the laser interferometers.

Figure 5 shows the experimental results of a zigzag motion profile. A commanded reference trajectory input to the controller is shown in Fig. 5(a), and the platen was controlled to follow the preplanned path. The measured trajectory from the Hall-effect

Table 1 Specifications of 2D-VH-11SO two-axis Hall-effect sensor [9]

Item	Test conditions	Typical value
Input resistance	$B=0$ mT, $I_c=2$ mA	22 k Ω
Output resistance	$B=0$ mT, $I_c=2$ mA	8.5 k Ω
Output voltage	$B=1$ T, $I_c=2$ mA	400 mV
Offset voltage	$B=0$ mT, $I_c=2$ mA	± 3 mV
Sensitivity	$I_c=2$ mA	400 mV/T
Magnetic sensitive volume		$0.25 \times 0.25 \times 0.20$ mm

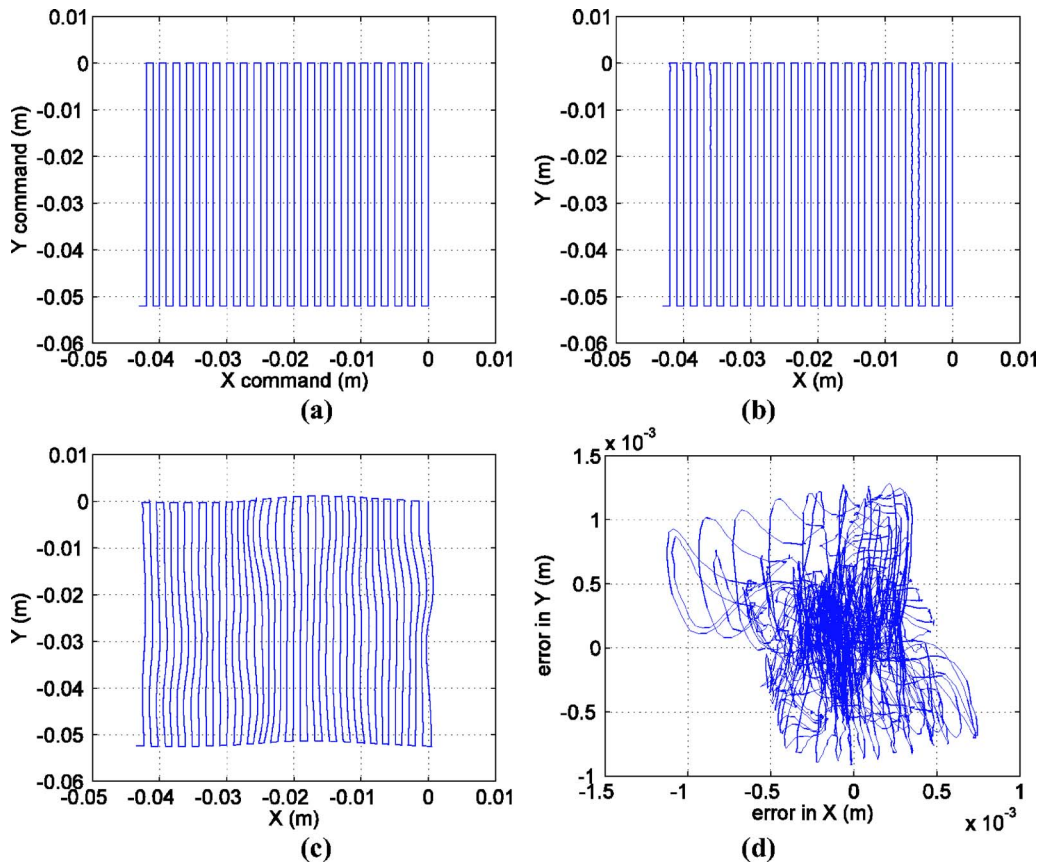


Fig. 5 Experimental results of 2-DOF positioning in X and Y following a zigzag trajectory. (a) Commanded trajectory, (b) measured trajectory from the Hall-effect sensors, (c) measured trajectory from the laser interferometers used for Hall-effect-sensor calibration purpose, and (d) error between the two measured values.

sensors shown in Fig. 5(b) is identical to Fig. 5(a) with an error below the resolution limit of our printer. However, the recorded position by the laser interferometers' outputs is shown in Fig. 5(c), which is believed to represent the actual motion profile of the platen much more faithfully. There is a significant deviation between the measurements from the laser interferometers and the outputs of the GLSDC based on the Hall-effect sensors' outputs. The maximum translational positioning error can be as large as 1.4 mm, as shown in Fig. 5(d). The main source of this error is believed to be the modeling error (as shown in Fig. 3(c)) originated from the nonideal fabrication and assembly listed in Sec. 4.1.

To improve the positioning accuracy, we have performed calibration by storing the positioning error of Fig. 5(d) in a two-dimensional lookup table. This was done because the outputs of the GLSDC are absolute and repeatable. The tabulated error was then compensated for using linear interpolation with the laser interferometer output as the "true" measurements. The results for a 4 mm step response in Fig. 6 show a significant reduction in positioning error after the sensor calibration and the error correction were performed. The noncalibrated result in Fig. 6(a) shows that the positioning error was as large as 300 μm whereas the calibrated and error-corrected result in Fig. 6(c) exhibits little steady-state positioning error with a position noise of 5 μm rms. We also present the laser-interferometer reading from the same step response in Fig. 6(b) for comparison. Comparing Figs. 6(b) and 6(c), the Hall-effect sensing scheme exhibits a positioning error of 17 μm , which is believed to be the "true" error after the sensor calibration and error correction. Thus this is a factor-of-20 reduction in positioning error compared to the noncalibrated case.

7.2 3 DOF Positioning Results. For 3 DOF positioning, all three Hall-effect sensors (sensors A , B , and C) were used and laser interferometers were not used in the control routine. Theoretically, two sensors are sufficient to control the 3 DOF motions, but due to the Hall-effect sensors' noise, it was difficult to keep the GLSDC algorithm from converging to a wrong value, which would result in instability. Having redundant sensor readings allows the GLSDC algorithm to be more likely to converge correctly, and hence makes it be a more stable sensing method. Three-dimensional look-up tables were not implemented because there was no feasible method to obtain position and orientation data with the conventional laser interferometers. The whole system would go unstable if moved with large rotation due to the laser-interferometry's fundamental limitation. If such a method would exist, a look-up table would likely improve the position resolution and, further, this GLSDC algorithm would not be necessary for such purpose.

The closed-loop responses to 10 μm and 100 μrad consecutive step commands are shown in Fig. 7. The steps can clearly be identified. This proves that the Hall-effect sensors are capable of detecting the changes in the magnetic flux density as the position changes less than 10 μm . Hence our sensing method based on the two-axis Hall-effect sensors has better than 10 μm translational position resolution and 100 μrad angular position resolution.

Figure 8 shows our sensing methodology's capability of detecting and controlling large rotational motion, from 0 to -0.12 rad (6.9 deg) and from 0 to 0.16 rad (9.2 deg). This is a factor-of-100 improvement in rotational sensing range compared with that of commercial laser interferometers. Further, since our sensing

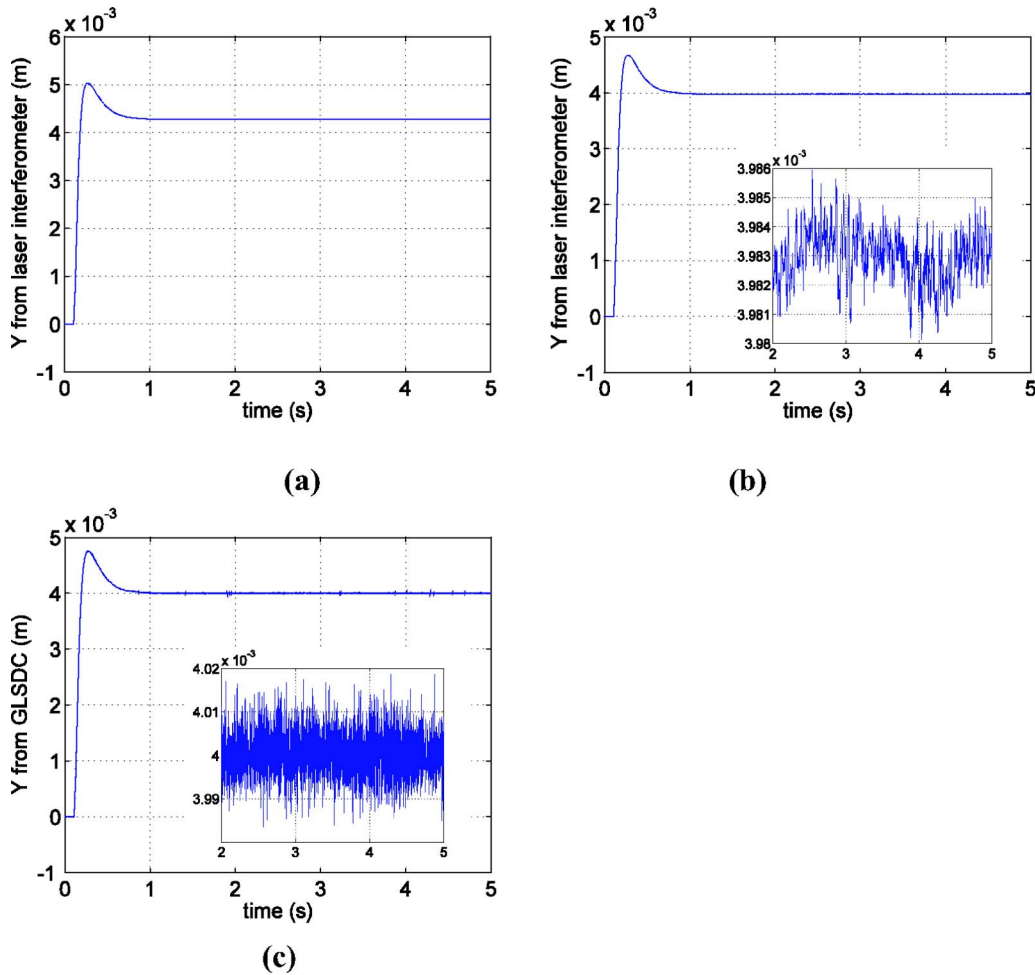


Fig. 6 Laser interferometer readings from a 4 mm step response (a) before calibration and (b) after calibration and error correction. (c) GLSDC output after calibration and error correction.

method is an absolute position-sensing scheme, the platen will always settle at the desired position and orientation regardless of its initial position.

Although this method has unrestricted rotational sensing range theoretically, the practical limitation comes from the following factors: (1) Our current setup uses planar actuators where they are modeled using the small-Euler-angle assumption. The controllers designed under this assumption will not work for large rotation due to significant modeling error. (2) The positions of the mounted sensors are known with a 100- μm -order precision, and hence large rotation can result in significant error. These two factors might also contribute to the fluctuation in the middle of the large rotational motion shown in Fig. 8(b) at around $t=1$ s. However, the controllers were robust enough to eliminate this angular position fluctuation quickly, and the positioner could complete the commanded angular ramp motion without losing stability.

8 Conclusions

We developed a novel multi-DOF position sensing mechanism using two-axis Hall-effect sensors that have the capability to detect the position with a micrometer-order resolution above any type of magnet matrix. The sensing mechanism and its experimental verification were presented in this paper. A GLSDC algorithm to process the raw Hall-effect sensor outputs and to resolve the position was implemented in real-time C codes at a sampling frequency of 800 Hz. The overall performance of the sensing methodology can be improved by using a faster DSP for the real-time

control, which can shorten the computational time required to close the control loop and increase the sampling rate.

Experimental results for 2 DOF and 3 DOF positioning were presented. For 2 DOF positioning, two sets of two-axis Hall-effect sensors were used to control the translational motion, laser interferometers were used to control the rotation, and we demonstrated a translational positioning resolution of better than 10 μm . The GLSDC outputs were calibrated against laser-interferometer readings, where the position error was mapped and stored in a two-dimensional lookup table. Error correction by linear interpolation improved the positioning accuracy significantly, reducing the maximum positioning error from 300 to 17 μm . This error can be further reduced by implementing redundant sensors and obtaining improved position least-squares estimates, which would allow this algorithm to converge more accurately.

For 3 DOF positioning, which relies exclusively on the Hall-effect sensors and where laser interferometers were not used, closed-loop consecutive step responses exhibited better than 10 μm translational and 100 μrad angular positioning resolutions. With our current configuration, we achieved rotations under closed loop as large as 16 deg, a factor-of-100 improvement compared with the conventional laser interferometry's rotational travel range. Theoretically this sensing methodology has unrestricted planar sensing range. Although there is a compromise in the sensing resolution, this sensing algorithm calculates the absolute position, whereas methods using laser interferometers give relative

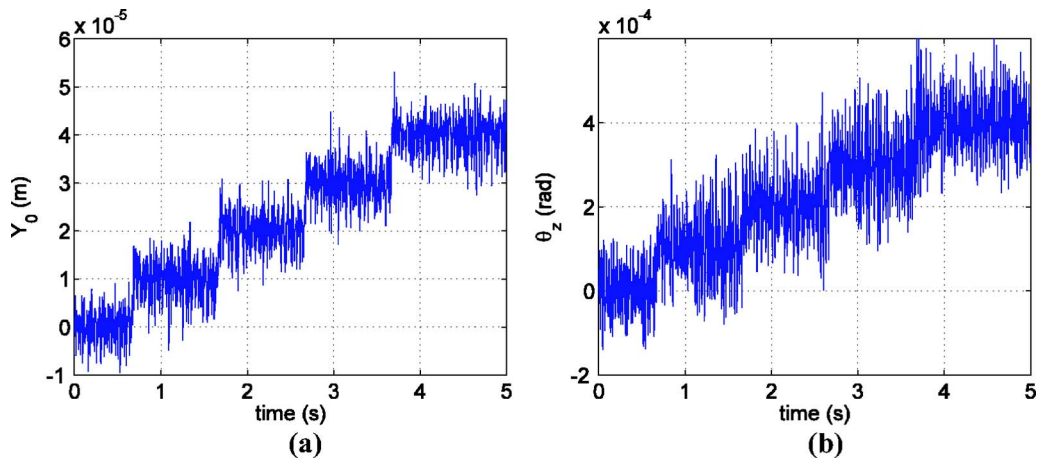


Fig. 7 Experimental results of positioning the platen in 3 DOFs using the proposed sensing methodology for (a) 10 μm consecutive steps in Y and (b) 100 μrad consecutive steps in θ_z

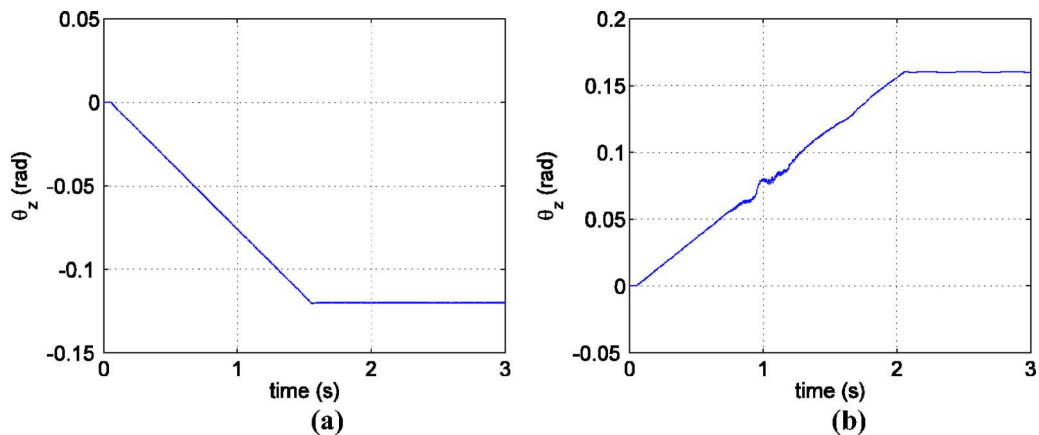


Fig. 8 Large-rotation ramp response in θ_z with (a) clockwise ($-\theta_z$) and (b) counter-clockwise ($+\theta_z$) motions

position with respect to its initial position. This is important in applications such as micro-assembly, where repetitive motion is required in the absolute position.

This sensing mechanism can also be used as a backup purpose when the sensing signals from laser interferometers become undetectable due to large rotation. The cost of our sensing mechanism as a stand-alone 3 DOF position sensor is only 1/200 of that of the commercial laser interferometry. We demonstrated in this paper that this sensing methodology can be employed in planar micro-positioning applications with unrestricted three-axis travel ranges.

Acknowledgment

This work was supported in part by the Texas Advanced Technology Program under Grant No. 000512-0225-2001. The authors thank Tiejun Hu, Nikhil Bhat, and Jie Gu, former graduate students of Won-jong Kim, for their contributions in this project.

References

- [1] Kim, W.-J., 1997, "High-Precision Planar Magnetic Levitation," Ph.D. dissertation, Massachusetts Institute of Technology, Cambridge, MA.
- [2] Kim, W.-J., Bhat, N., and Hu, T., 2004, "Integrated Multidimensional Positioner for Precision Manufacturing," *J. Eng. Manuf.*, **218**(4), pp. 431–442.
- [3] Shan, X., Kuo, S.-K., Zhang, J., and Menq, C.-H., 2002, "Ultra Precision Motion Control of a Multiple Degrees of Freedom Magnetic Suspension Stage," *IEEE/ASME Trans. Mechatron.*, **7**(1), pp. 76–78.
- [4] Holmes, M., Hocken, R., and Trumper, D. L., 2000, "The Long-Range Scanning Stage: A Novel Platform for Scanned-Probe Microscopy," *Precis. Eng.*, **24**(3), pp. 191–209.

- [5] Jung, K. S., and Baek, Y. S., 2003, "Precision Stage Using a Non-contact Planar Actuator Based on Magnetic Suspension Technology," *Mechatronics*, **13**, pp. 981–999.
- [6] Gan, W.-C., and Cheung, N. C., 2003, "Development and Control of a Low-Cost Linear Variable-Reluctance Motor for Precision Manufacturing Automation," *IEEE/ASME Trans. Mechatron.*, **8**(3), pp. 326–333.
- [7] Slocum, A. H., 1992, *Precision Machine Design*, Prentice-Hall, Englewood Cliffs, NJ.
- [8] Schott, C., Racz, R., Betschart, F., and Popovic, R. S., 2002, "A New Two-Axis Magnetic Position Sensor," *Sensors*, **2**, pp. 911–915.
- [9] Law, L., 2003, "Measuring Current With IMC Hall Effect Technology," *Sensors*, **3**(11), pp. 29–32.
- [10] Driljace, P., Demierre, M., Schott, C., and Popovic, R. S., 2002, "Nonlinear Effects in Magnetic Angular Position Sensor With Integrated Flux Concentrator," *Proc. 23rd International Conference on Microelectronics*, Vol. 1, pp. 223–226.
- [11] Trontelj, J. Jr., 2001, "Functionality Test for Magnetic Angular Positioning Integrated Circuit," *Informacije MIDE M*, **31**(4), pp. 287–289.
- [12] Trumper, D. L., Kim, W.-J., and Williams, M. E., 1997, "Magnetic Arrays," U.S. Patent 5,631,618, May 20.
- [13] Halbach, K., 1980, "Design of Permanent Multipole Magnets With Oriented Rare Earth Cobalt Material," *Nucl. Instrum. Methods*, **169**(1), pp. 1–10.
- [14] Hu, Y. H., and Hwang, J.-H., 2002, *Handbook of Neural Network Signal Processing*, CRC, Boca Raton, FL.
- [15] Crassidis, J. L., and Junkins, J. L., 2004, *Optimal Estimation of Dynamic Systems*, Chapman & Hall/CRC, Boca Raton, FL.
- [16] Asakawa, T., 1995, "Two Dimensional Precise Positioning Devices for use in a Semiconductor Apparatus," U.S. Patent 4,535,278, Aug. 13.
- [17] Hinds, W., 1987, "Single Plane Orthogonally Movable Drive System," U.S. Patent 4,654,571, Mar. 31.
- [18] Ebihara, D., and Watada, M., 1989, "Study of a Basic Structure of Surface Actuator," *IEEE Trans. Magn.*, **25**(5), pp. 3916–3918.
- [19] Chitayat, A., 1999, "Two-Axis Motor With High Density Magnetic Platen," U.S. Patent 6,005,309, Dec. 21.